Ultrasonics 160 (2026) 107912

Contents lists available at ScienceDirect

Ultrasonics

journal homepage: www.elsevier.com/locate/ultras

On the existence of local defect resonance in ultrasonic guided waves interaction with horizontal defects in plates

Mingyue Zhang [a,b], Sandrine Tahina Rakotonarivo [c], Antonino Spada [d], Margherita Capriotti [a,*]

[a] Aerospace Engineering Department, San Diego State University, 5500 Campanile Drive, San Diego, CA, 92182, United States
[b] Structural Engineering Department, University of California San Diego, 9500 Gilman Drive, La Jolla, CA, 92093, United States
[c] Aix Marseille University, CNRS, Centrale Marseille, LMA, 4 impasse Nikola Tesla, Marseille, 13453, France
[d] Department of Engineering, University of Palermo, Viale delle Scienze, Palermo, PA, 90128, Italy

ARTICLE INFO

Keywords:
Local defect resonance
Ultrasonic guided waves
Nondestructive evaluation
Free vibrations
Computational NDE
Horizontal defect

ABSTRACT

The interaction of ultrasonic guided waves with defected structures gives rise to local defect resonance (LDR), which manifests in large displacements in the vicinity of the defect and affects the reflection and transmission spectra. This paper investigates the fundamental mechanism at the origin of the LDR phenomenon in isotropic elastic plates, using a hybrid computational method (Global–Local). The analyses show that the coupling of ultrasonic guided waves with the vibrational resonance modes of the sub-structure, geometrically defined by the defect, causes LDR, and boundary conditions affect it secondarily. The coupling mechanism is captured by the Global–Local method and is investigated in relation to the characteristics of the defect and the relationship to the host-structure. The coupling occurs at defect lengths that are odd multiples of the modes' quarter wavelengths. Comparisons with analytical, finite element and methods in literature for the computation of the natural and LDR frequencies are provided. The presence of LDR and its effect on broadband reflection and transmission ultrasonic spectra away from the defected region are also verified experimentally and can be used for remote defect characterization in NDE applications. These studies clarify the fundamental understanding of LDR and provide an effective approach to capture and predict LDR in ultrasonic guided wave propagation in plate-like structures.

1. Introduction

Among the ultrasonic methods for damage detection, Ultrasonic Guided Waves (UGW) offer advantages, enabling fast, sensitive and cost-effective inspections. UGW are elastic waves that propagate in bounded geometries (i.e. waveguides) and provide full cross-sectional involvement while maintaining a wide inspection range [1]. Resonance phenomena in UGW propagation in structures arise due to different mechanisms. These can be due to phase matching and nonzero power flow conditions [2–4], zero group velocity [5,6], wave interaction with geometrical and boundary configurations of the waveguide [7] or with discontinuities [8], or a combination of the above [9].

When ultrasonic guided waves propagate in structures and encounter defects with specific configurations, multiple reflections can occur within the defect region, leading to substantial trapping of wave energy above, below, and between the defected areas until the energy eventually dissipates [10,11]. The phenomenon of local resonance in wave propagation is characterized by wave energy localizing and resonating within a defined region at specific frequencies, potentially indicative of structural anomalies. Rohklin [12] identified the cause of resonances by solving analytically the diffraction problem of Lamb waves in a plate with a finite crack. He stated that the crack region behaves as a high-Q resonator for the Lamb wavemodes reflected and mode-converted by the edges of the crack. Solodov et al. [13–15] proved experimentally that defects exhibit resonances when subjected to forces matching their natural frequencies. The work also named the phenomenon “local defect resonance” (LDR).

Prior work on LDR can be categorized into three methodological directions: analytical, numerical, and experimental investigations. On the analytical side, trapped-mode phenomena in plates have been investigated via point-eigenvalue analyses of the spectrum using Wiener–Hopf and related techniques [8,16–19], and more recently by complex modes expansion with vector projection (CMEP) method [20]. On the numerical side, conventional finite-element formulations [21,22] and time domain spectral finite element (TSFE) method [23] are widely used, but

* Corresponding author.
E-mail address: mcapriotti@sdsu.edu (M. Capriotti).

https://doi.org/10.1016/j.ultras.2025.107912
Received 18 April 2025; Received in revised form 31 October 2025; Accepted 24 November 2025
Available online 25 November 2025

can be computationally demanding for parametric studies. To improve efficiency and maintain accuracy, hybrid/semi-analytical approaches have been developed, including the use of Semi-Analytical Finite Element (SAFE) method combined with normal mode expansion method (NME) [24], boundary integral equation methods (BIEM) [22], semi-analytical hybrid approaches (SAHA) that couple BIEM with frequency-domain SEM (FEDSEM) [25], modal-expansion model [26], and the Modal Decomposition Method (MDM) [27]. Experimental validation of LDR phenomenon has been reported using different techniques, including thermography methods [28], resonant airborne acoustic activation combined with vibrometry [15], air-coupled ultrasonic system [21], and most commonly, by the use of laser Doppler vibrometer (LDV) [22, 29–34]. These experimental studies corroborate the existence of discrete resonances and spatial energy trapping predicted by theory and simulation.

Despite this substantial body of work, important gaps remain. Prior studies consistently indicate that LDR features – most notably the resonance frequencies – depend on defect characteristics such as size, location and type [14,22,23,27]. However, a generalizable, mechanism-based framework that quantitatively maps LDR observations to defect parameters remains limited: analytical models typically require strict geometric/constraint assumptions, whereas high-fidelity numerical approaches, though broadly applicable, can be computationally expensive for parametric exploration. Moreover, most experimental demonstrations acquire measurements directly on top of the defect, providing limited evidence for remote detection that is more representative of practical NDE/SHM scenarios.

To address these limitations, the present work employs a hybrid Global–Local (GL) formulation that couples a semi-analytical waveguide description of the surrounding pristine plate to a high-resolution finite element model of the defected local zone. Using this method, this work furthers the understanding of the LDR phenomenon arising in UGW interactions with horizontal defects in elastic plates and investigates the mechanism at its cause. In Section 2, the hybrid Global–Local method is presented as an efficient solution to compute broad scattering spectra of UGW modes that capture how LDRs manifest in transmission and reflection. Section 3 reviews the nature of LDRs as due to the coupling of propagating UGW with normal modes of vibrations and makes the defect length-to-wavelength relationship explicit. The analytical and numerical solutions of the normal modes of vibrations for the presented case study are reported in the Appendix. Section 4 provides an experimental demonstration of the numerical studies, observing the LDR phenomenon in the ultrasonic range, and showing its effect on UGW reflection and transmission away from the defect. A discussion on the boundary conditions of coupling and the influence of waveguide parameters on LDR computation follows in Section 5. Further analyses on the quantitative relations between resonances and defect parameters are studied in depth in a following paper, focusing on practical NDE applications.

2. Local defect resonance by hybrid global–local method

The complex propagation and interactions associated with UGW present substantial challenges in understanding the resulting waveforms, hence in signal interpretation. Advanced modeling techniques are needed to capture their behavior accurately, comprehensively and efficiently.

Hybrid methods enable accommodating any geometrical discontinuity or defect in the scattering problem and provide accurate solutions with reduced computational demands. They have proven invaluable in enabling accurate and efficient simulations of UGW, particularly at ultrasonic frequencies [25,35–40].

The hybrid Global–Local method is utilized to simulate UGW propagation within waveguides containing defects and/or discontinuities along the wave propagation direction. In this approach, the waveguide is partitioned into global and local regions. The global portion represents the pristine structure, while the local part contains the discontinuity. Specifically, the 2D model discretizes the x-z plane, where x is the wave propagation direction, and z corresponds to the thickness direction. The model adopts plane strain assumption, considering the 2D transverse section as infinite in the y-direction. A detailed formulation of this method is described in [36].

Within this framework, an incident time-harmonic guided wave travels along the wave propagation direction. The wave is scattered into reflected and transmitted waves after interacting with the discontinuity within the local region. By ensuring displacement compatibility and forces equilibrium at the boundaries between the global and local regions, the hybrid solution is effectively extracted. The 2D scattering problem is visually depicted in Fig. 1.

The waveguide under consideration in this work is a 2 mm aluminum plate. Given that evanescent modes are excluded from the analyses performed in this paper, the local zone (LZ) remains fixed across all tests, with a length of 50 mm. This size considerably exceeds the minimum requirement of local zone boundary/defect distance being more than four times the plate thickness, as established in [41]. A minimum of 20 elements per wavelength is considered sufficient to ensure computational accuracy [36,42]. In this work, each finite element within the local zone is a linear element with four Gauss points and quadrilateral shape, with a mesh size of 0.05 mm, equating to 40 elements through the thickness, and 40,000 elements in total, in the pristine case.

The local-zone configurations of off-centered horizontal defects in the aluminum plate and their scattering spectra are presented in Fig. 2(a) and (b). In Fig. 2(a), a 20 mm long off-centered delamination with a depth of 0.5 mm is modeled by separating the finite element nodes (infinitesimal thickness horizontal defect), following established practice [43,44]. In Fig. 2(b), a notch with the same length and remaining depth is modeled by removing elements. For each configuration, the normalized scattered energy at the local-zone boundaries is computed for the fundamental anti-symmetric ($A0$) incident mode across a 0–200 kHz frequency spectrum with step $df = 1$ kHz. This work focuses exclusively on the $A0$ incident mode in both the numerical simulations and experiments; analyses of $S0$ incidence are outside the present scope and will be reported separately.

In the delamination case (Fig. 2(a)), when the $A0$ is incident, most of the energy is transmitted (solid line) in the same mode, except for highly localized sharp transmission drops at specific frequencies, with negligible $A0 \rightarrow S0$ conversion across the spectrum. In the notch case (Fig. 2(b)), most of the energy is reflected and substantial $A0 \rightarrow S0$ mode conversion is observed; at the resonance frequencies, the reflection exhibits sharp drops. Interestingly, the resonance frequencies closely match those of the delamination with the same sub-laminate, as quantified in Table 7, and further discussed in Section 5.2. For clarity, resonance frequencies in this section are analyzed using the delamination configuration, in which pronounced frequency peaks and negligible mode conversion are observed.

At these resonance frequencies (highlighted in red), interaction of UGW with the boundaries and discontinuities within the structure leads to the formation of standing wave patterns or energy vortices that persist after the initial wave excitation has ceased. In the delamination configuration, the localized energy prevents transmission creating narrow bandgaps in the frequency domain. The magnitude of such energy drops varies at different frequencies: for example, the transmission drop at 84 kHz is relatively small (~10%), while at 7 kHz, the normalized energy significantly drops from 1 to 0. Two groups of resonance frequencies, characterized by in-plane and out-of-plane motion respectively, are present, as noted in previous research [22]. Most of the resonance frequencies identified are dominated by out-of-plane motion. An additional energy drop is observed at 130 kHz in the delamination case, but this resonance is not considered in this study as it is primarily characterized by in-plane motion.

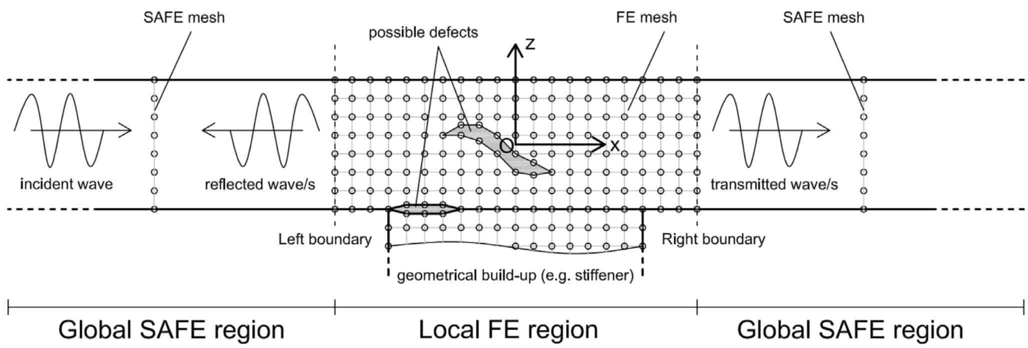

Fig. 1. Geometrical representation of the scattering of an incident wave in reflected and transmitted waves from a discontinuity within the local zone (LZ), with indication of the adopted discretization strategies in each region of the Global–Local (GL) approach [36].

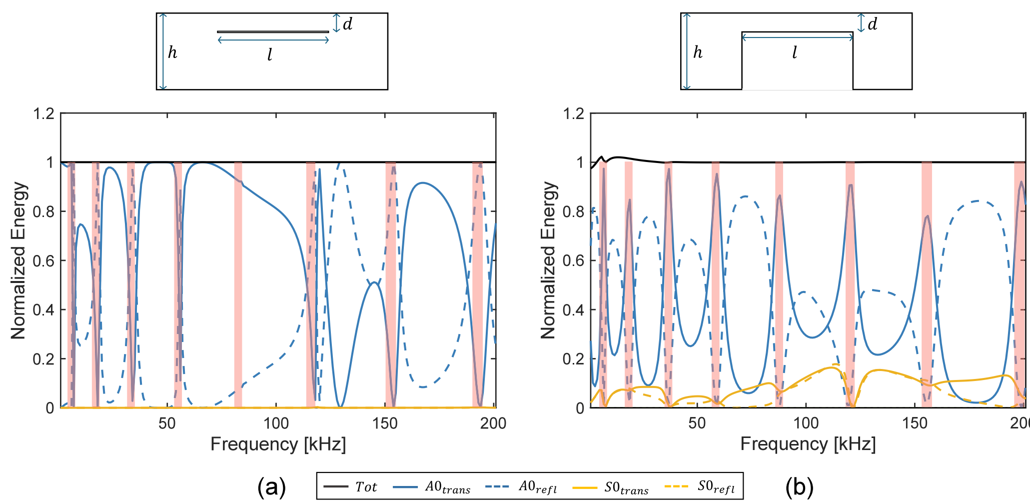

Fig. 2. Off-centered horizontal defects in a 2 mm aluminum plate: (a) GL local-zone configuration showing a top-surface delamination (l = 20 mm, d = 0.50 mm; not to scale) and the corresponding normalized energy scattering spectra for $A0$ incident mode, with resonance frequency peaks highlighted; (b) GL local-zone configuration showing a notch (l = 20 mm, depth d = 0.50 mm; not to scale) and the corresponding normalized energy scattering spectra for $A0$ incident mode, with resonance frequency peaks highlighted.

The resonance peaks are attributed to the LDR phenomenon, as they arise from the interaction between propagating guided modes matching the natural modes of vibration of the region (i.e. sub-waveguide) defined by the defect. These observations align with findings from prior research [22,24,27] and emphasize the capability of the method in capturing the LDR phenomenon.

3. Local defect resonance as ultrasonic guided waves - vibrational modes coupling

To elucidate the LDR phenomenon, the interaction of the guided wave modes with the sub-waveguide's natural modes of vibration is here made explicit and analyzed.

When Lamb waves propagate through a structure with delamination, they interact with the edges of the delaminated region, leading to multiple reflections and trapping energy within the defective area [12,33,43,45–48]. This phenomenon is characterized by a significant amount of wave energy being confined within the sub-laminates separated by the delamination, generating trapped modes.

The trapped modes dynamically interact with the intrinsic free vibrational characteristics of the sub-structure. This interaction results in coupling UGW modes to normal vibrational modes, causing resonance at the sub-laminate's natural frequencies. This influences the resulting wave propagation.

To clarify the mode coupling between UGW trapped modes and normal modes, a representative case involving the 20 mm long, 0.5 mm deep off-centered delamination within the aluminum plate (host waveguide) is analyzed, as depicted in Fig. 3. Several other cases have been studied by the authors with similar results and will be reported in a following work. The LDR frequencies of UGW were obtained from the Global–Local method, as described in Section 2. These results are here compared with the LDR frequencies reported by Eremin et al. [22], who employs the Boundary Integral Equation Method (BIEM) and the Finite Element Method (FEM) for the numerical approximation of eigenfrequencies (i.e. resonance frequencies) in UGW propagation in defected plates. The LDR frequencies from UGW propagation in the delaminated plate (Fig. 3(a) and (b)) are then compared to the natural frequencies of normal modes of vibrations of the sub-laminate only (sub-structure, Fig. 3(c) and (d)) above the delamination. These natural frequencies are obtained via both analytical calculations (1D sub-structure, a two-end fixed Euler–Bernoulli beam) and FEM (3D sub-structure). The Appendix reports the analytical vibration solutions and 3D FEM modeling.

Table 1 presents the first six LDR frequencies of the delaminated aluminum plate, obtained from the Global–Local method, alongside those reported in literature using BIEM and FEM [22]. The table also displays the natural frequencies of the normal modes of free vibration of the thinner sub-laminate alone, segmented by the delamination. These natural frequencies are computed using ABAQUS shell S4R elements (dx = dy = 0.25 mm) and solid C3D8 elements (dx = dy = 0.2 mm, dz = 0.1 mm), with clamped boundary conditions on all four edges and 3D structure. The analytical solution, as described in the Appendix, is also provided.

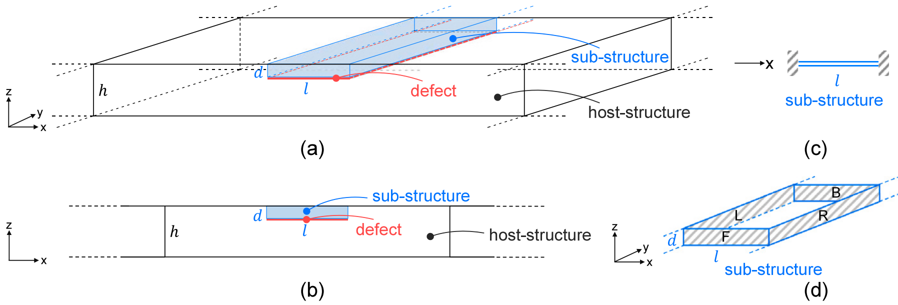

Fig. 3. (a) 3D full problem, (b) 2D Global–Local configuration, (c) 1D sub-structure (two-end fixed Euler–Bernoulli beam), and (d) sub-structure in 3D FEM modeling (F, B = front and back edges; L, R = left and right edges).

Table 1
Comparison of LDR frequencies (kHz) of the first six modes in the delaminated plate obtained from the GL (df = 1 kHz) method and literature (BIEM and FEM, [22]) with natural frequencies of the thinner sub-laminate computed from the analytical and numerical (ABAQUS S4R and C3D8) solutions.

Mode	LDR frequencies (kHz)			Natural frequencies (kHz)		
	GL	BIEM	FEM	Analytical	S4R	C3D8
1	7.00	6.93	6.88	6.50	6.80	6.77
2	18.00	18.41	18.37	17.91	18.65	18.58
3	34.00	34.54	34.46	35.10	36.29	36.21
4	56.00	55.83	55.72	58.02	59.46	59.38
5	84.00	84.39	84.20	86.68	87.89	87.83
6	118.00	118.75	118.41	121.06	121.31	121.26

Fig. 4 provides a visual representation of the data presented in Table 1, comparing the LDR frequencies and natural frequencies of the first six modes. The plots highlight the close alignment between the results obtained from the Global–Local method (horizontal dashed line) and the literature, as well as with the natural frequencies computed from both the analytical and numerical solutions. In particular, among the solutions for the LDR, the Global–Local results closely match the literature results from both BIEM and FEM, with the maximum discrepancy verified at the first mode (relative error below 2%). With respect to the natural frequencies, the maximum relative error is observed in comparison with the S4R FEM, which shows a 6.74% error in the third mode. However, the relative error diminishes at higher frequencies. It is also noted that the LDR frequencies obtained from Global–Local and reported in prior literature, closely match the natural frequencies of fixed-fixed beam (analytical and numerical) but are generally lower. This difference arises because the simplified fixed-fixed beam model is stiffer than the actual defect-defined sub-laminate embedded in the host plate.

The analytical solution for the normal modes of the sub-laminate, derived from Eq. (A.1), can be approximated using the asymptotic behavior of the characteristic equation. Specifically, as n increases, the solution $\beta_n l$ for each mode can be approximated by:

$$\beta_n l \approx \frac{(2n-1)\pi}{2} \tag{1}$$

where β_n is the wavenumber for the nth mode. The wavelength λ_n for the nth mode is defined as $\lambda_n = 2\pi/\beta_n$.

Consequently, the ratio of the sub-laminate width l to the wavelength λ_n for the nth mode can be expressed as:

$$\frac{l}{\lambda_n} = \frac{2n-1}{4}, \tag{2}$$

indicating that the width of the sub-laminate is an odd integer multiple of the quarter-wavelength of the nth mode. This relationship highlights the resonance conditions that occur when the width of the sub-laminate supports a standing wave structure with a specific number of quarter-wavelengths, a characteristic feature of the normal modes.

Table 2
Analytical and GL wavelengths (mm) and length ratios for thinner sub-laminate (l = 20 mm, d = 0.50 mm).

Mode	λ_n (mm)	λ_{A0} (mm)	$\frac{l}{\lambda_n/4}$	$\frac{l}{\lambda_{A0}/4}$
1	26.57	26.45	3.01	3.02
2	16.00	16.46	5.00	4.86
3	11.43	11.94	7.00	6.70
4	8.89	9.27	9.00	8.63
5	7.27	7.53	11.00	10.62
6	6.15	6.31	13.00	12.68

Table 2 validates these observations presenting a comparison between the wavelength λ_n of the normal modes obtained from the analytical solution and the wavelength λ_{A0} of the A_0 mode, computed using the Global–Local method, in correspondence of the LDR. The table also includes the corresponding values of the ratio $\frac{l}{\lambda/4}$ for both the analytical and A_0 resonance solutions.

The values in this table confirm that for each mode, the ratio $\frac{l}{\lambda/4}$ derived from the analytical solution corresponds to odd integers (3, 5, 7, etc.). Moreover, the comparison with the $A0$ resonances computed by the Global–Local method reveals strong agreement with the analytical solutions, with only minor deviations (within 4.5%) in both the wavelength and ratio values for each mode.

The resonance behavior of the sub-laminate is highly dependent on the width-to-wavelength ratio, particularly at odd integer multiples of $\frac{l}{\lambda/4}$.

4. Experimental validation

4.1. Experimental setup

To investigate the LDR phenomenon experimentally, a combined contact transducer in actuation and a non-contact Laser Doppler Vibrometer (LDV) in reception were used on a notched aluminum plate. Fig. 5(a) presents a schematic of the LDV scanning system setup; (b) shows a side view of the experimental arrangement; and (c) displays the top view of the tested aluminum specimen. LDV allows for high spatial and temporal resolution of the wavefield, and has proven to be an efficient and sensitive system for analyzing LDR phenomenon [14,15,24,27,31,49,50]. The tests were conducted in the Marine Physical Laboratory (Scripps Institute of Oceanography, University of California San Diego) where the LDV system was made available for this test. The experiments were conducted on a 2-mm-thick aluminum plate with dimensions of 610 mm × 610 mm. A notch defect, 6.5 mm in width and 1.6 mm in depth (0.4 mm remaining depth), was introduced along the plate's centerline, on the backside of the plate, for a

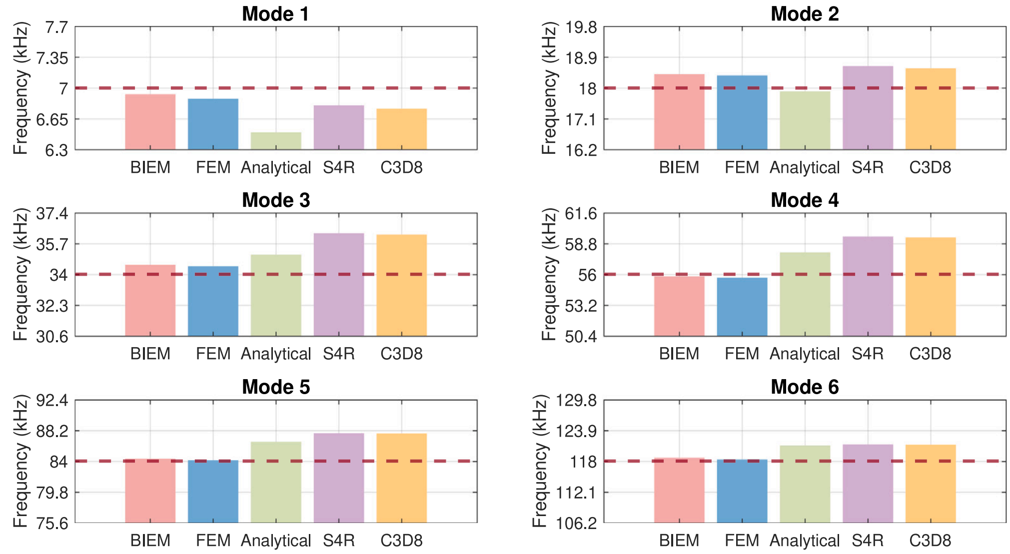

Fig. 4. Comparison of local and natural defect resonance frequencies for the first six modes in Table 1, illustrated by histograms for various methods. Dashed red line represents the GL method. Dynamic range varies for each plot (±10% about GL value).

length of 510 mm. To minimize elastic wave reflections from the plate boundaries, plasticine was applied along all four edges of the plate.

The broadband excitation was provided by a piezoelectric transducer (Picosensors, Mistras) placed on the front side of the plate [51]. The transducer was positioned at a distance of 228 mm from the center of the notch to maximize the inspected area and a broadband square pulse generated by a Pulser/Receiver (Olympus 5077PR) was used as excitation. The out-of-plane velocity, $v(x,t)$, of the plate surface was measured using the scanning LDV (OptoMET SWIR). Due to the limited bandwidth of the LDV, manual scanning was performed point by point for 256 mm along the x-direction (Fig. 5(c): laser scanning path x_1 = -128 mm to x_2 = 128 mm) with a spatial resolution of ∼1 mm. This resulted in a total of 257 measurement locations. At each location, averaging was performed (2087 waveforms) to enhance signal-to-noise ratio. The time duration of each signal was 2 ms.

4.2. Signal processing and visualization

The two-dimensional fast Fourier Transform (2D-FFT) was applied to the collected time-space LDV dataset (Fig. 6(a)) to transform the measured velocity $v(x,t)$ into the frequency–wavenumber domain: $V(k,w) = \mathcal{F}(v(x,t))$.

A 2D window function $W_{f/b}(k,w)$ in the frequency–wavenumber domain is introduced as a filter to separate the wave propagation directions [52–54]. The filter is designed to separate forward (outgoing) waves $\widetilde{V}_f(k,\omega)$ from backward (incoming) waves $\widetilde{V}_b(k,\omega)$ as:

$$\widetilde{V}_{f/b}(k,\omega) = V(k,\omega)\cdot W_{f/b}(k,\omega) \tag{3}$$

where the forward and backward propagation windows are defined as:

$$W_f(k,\omega) = \begin{cases} 1, & \text{for } k\cdot\omega > 0, \\ 0, & \text{otherwise.} \end{cases} \qquad W_b(k,\omega) = \begin{cases} 1, & \text{for } k\cdot\omega < 0, \\ 0, & \text{otherwise.} \end{cases} \tag{4}$$

Prior filtering, three spatial regions of interest were distinguished along the x direction (Fig. 5(c)): Region 1, as the pristine region before the defect (x = −128 mm to −20 mm) ; Region 2, as the defect region (x = −3 mm to 3 mm); Region 3, as the pristine region after the defect (x = 20 mm to 128 mm). This was done to remove the effect of the LDR on top of the defect and isolate its effect on the reflected and transmitted waveforms. The filtered wavefield $\widetilde{V}(k,\omega)$ is then separated into forward and backward propagating components, and reconstructed for Region 1 and Region 3. Incident waves are defined as the forward-propagating waves in Region 1; reflected waves are defined as the backward-propagating waves in Region 1; transmitted waves are defined as the forward-propagating waves in Region 3.

Fig. 6(b), (c), and (d) show the incident, reflection and transmission spectrum, respectively. Fig. 6(b) also overlays the dispersion curve of the $A0$ mode, obtained from the Global–Local method [36], on the 2D spectrum $\widetilde{V}_f(k,\omega)$. The dispersion curve demonstrates good agreement with the experimental results. Frequency content above 250 kHz is excluded, due to the bandwidth of the transducer in excitation. In Fig. 6(c), amplitude gaps are observed at approximately 50 kHz, 125 kHz and 240 kHz. These drops provide evidence of LDR frequencies in reflection arising from the phenomenon. Conversely, waves are present only at those same frequencies, in transmission (Fig. 6(d)).

The same frequency–wavenumber filtering and analysis procedure is applied to separate the forward and backward propagating waves across the entire plate. Subsequently, an inverse Fourier Transform is performed along the wavenumber (k) direction. The resulting velocity amplitude profiles, $v(x,f)$, are presented in Fig. 7(a) and (b) for the forward and backward propagating waves respectively.

After interacting with the defect, most of the wave propagation is blocked, except for specific frequencies (Fig. 7(a)), corresponding to the LDR frequencies, that transmit in the forward propagation direction past the defect (Region 3). Conversely, most of the waves are reflected (Region 1), except at these specific frequencies (Fig. 7(b)). Within the defect region (Region 2), waves are trapped and show high amplitude particularly at the LDR frequencies. Three LDR frequencies are expected to be observed as in Fig. 6. However, due to the frequency range limitations of the transducer, only the second LDR frequency is mainly visible in this 2D representation, as highlighted in Fig. 7(a) and (b).

To better identify and evaluate the exact LDR frequency values and compare them with Global–Local results, normalized scattering spectra in reflection and transmission are extracted over the frequency domain. The spectra coefficients are derived from the mean velocity amplitudes of the reflected and transmitted waves, normalized by the incident wave amplitude. The process is described as follows:

$$v_{\text{mean}}(f) = \frac{1}{x_2 - x_1}\int_{x_1}^{x_2} |v(x,f)|\,dx \tag{5}$$

where $[x_1, x_2]$ represent the spatial bounds of the region, as defined in Fig. 5(c). This computation is performed for the incident, reflected and transmitted spectra, respectively, away from the defect.

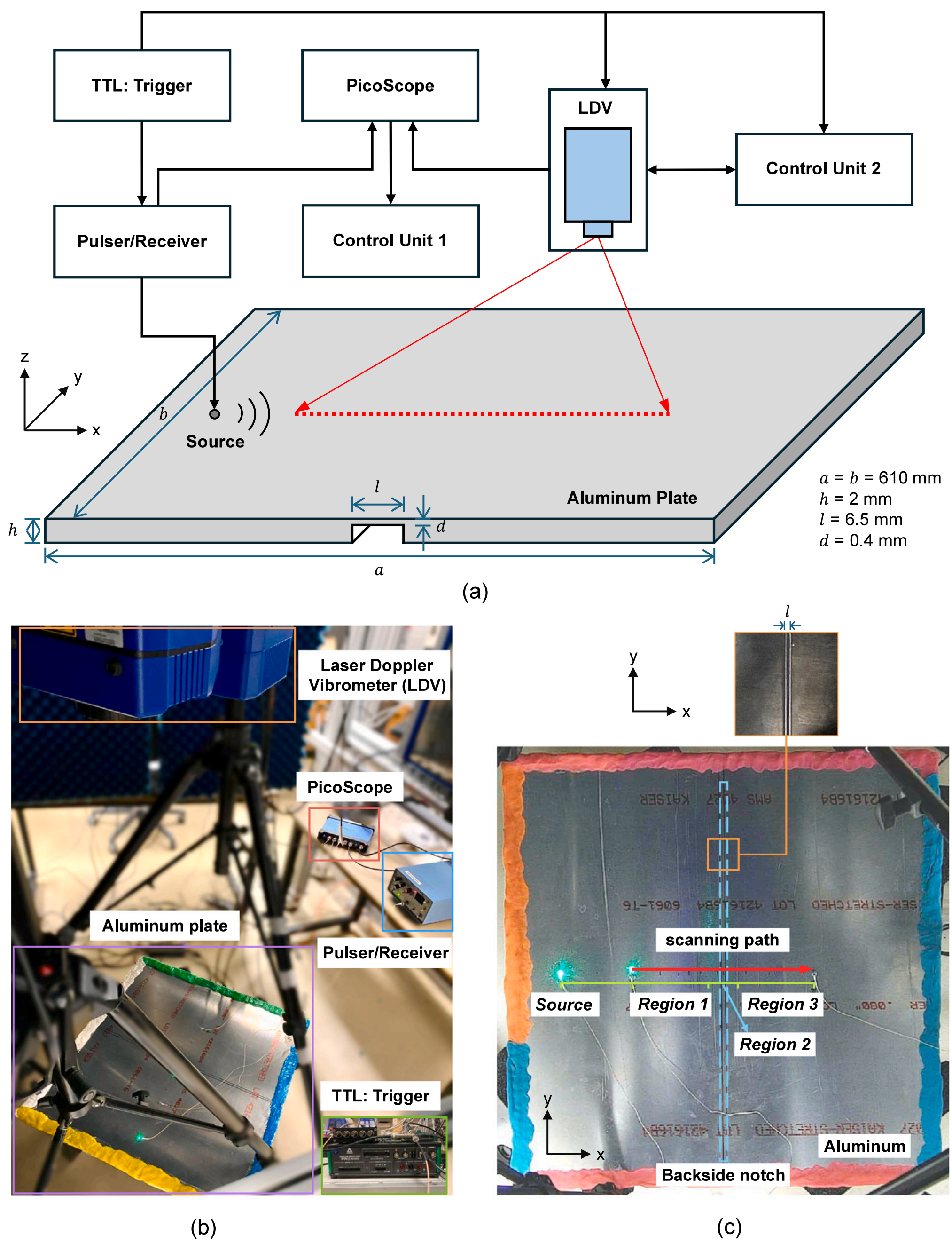

Fig. 5. Experimental setup: (a) schematic of the LDV scanning system, (b) side view of the test configuration, and (c) top view of the specimen, showing the source location at $x = -228$ mm. The scanning region is divided into three regions: Region 1 (x = −128 mm to −20 mm, before the defect), Region 2 (x = −3 mm to 3 mm, defect region), and Region 3 (x = 20 mm to 128 mm, after the defect).

The normalized scattering coefficients are defined as the ratio of the mean velocity amplitudes reflected and transmitted to the incident one:

$$\kappa_{\text{refl}}(f) = \frac{v_{\text{mean, refl}}(f)}{v_{\text{mean, inc}}(f)}, \kappa_{\text{transm}}(f) = \frac{v_{\text{mean, transm}}(f)}{v_{\text{mean, inc}}(f)} \tag{6}$$

The obtained normalized scattering spectra are presented in Fig. 8(a) and compared with the results computed by the Global–Local method (notch l = 6.5 mm, d = 0.4 mm) in Fig. 8(b). The experimental results show excellent agreement with the predicted Global–Local results up to 250 kHz, which corresponds to the frequency range limitation of the transducer used in the test. Three LDR frequencies (48 kHz, 123 kHz, and 237 kHz) are observed clearly and align closely with the frequencies of 48 kHz, 123 kHz, and 235 kHz predicted by Global–Local method. The large amplitude peaks noticeable in the lower frequency range (below 15 kHz) are attributed to the frequency range limitations of the transducer at those frequencies.

The experimental configuration presented in this study focuses on a notch defect. A detailed discussion of LDR frequencies in plates with various defect types is provided in the next section.

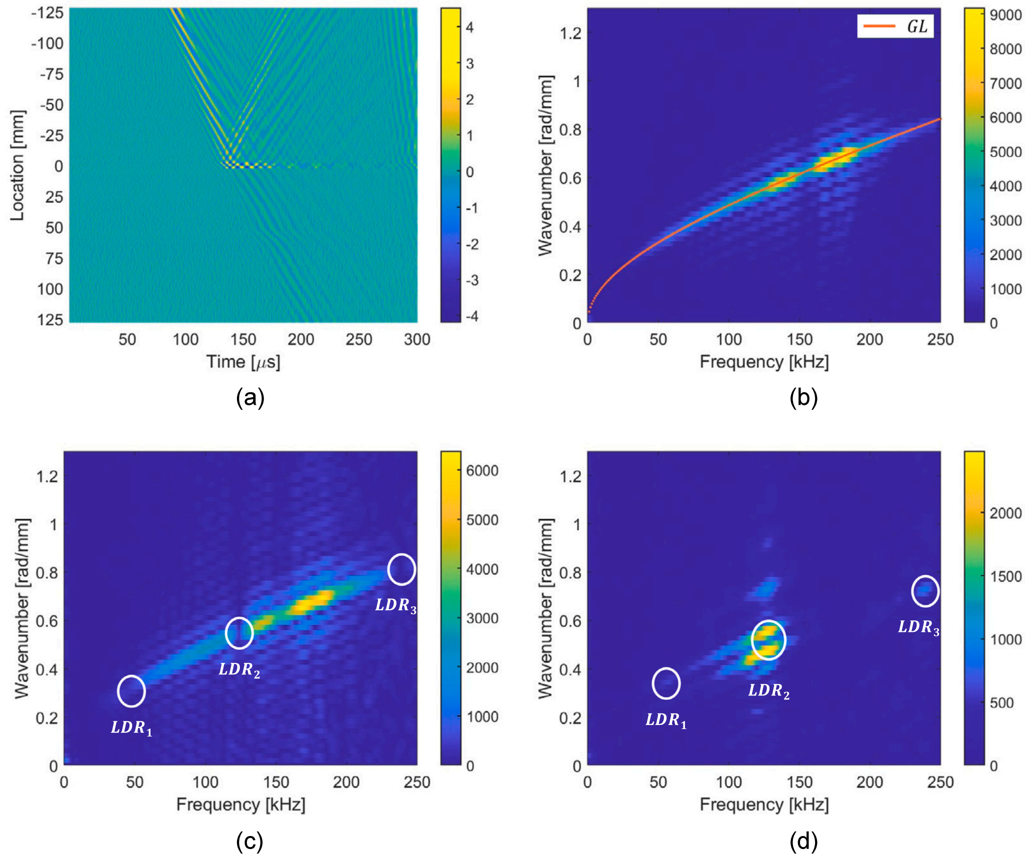

Fig. 6. (a) Surface velocity $v(x,t)$ obtained from LDV. Filtered and reconstructed frequency–wavenumber spectra for (b) incident waves (forward propagation in Region 1), (c) reflected waves (backward propagation in Region 1), and (d) transmitted waves (forward propagation in Region 3). All spectra are reported in the positive frequency–wavenumber domain for ease of comparison.

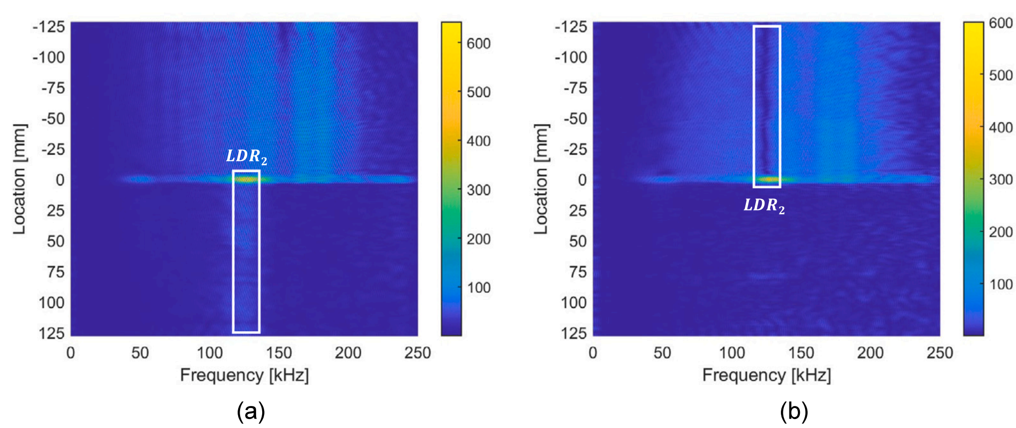

Fig. 7. Filtered and reconstructed frequency-space spectrum at locations across the entire plate: (a) forward propagation and (b) backward propagation.

5. Discussion

The Global–Local method captures LDR when solving for UGW propagation in a structure with defects (e.g. plate with horizontal defects). When comparing this solution with that obtained for the normal modes of free vibration, it is noted that the frequencies at which local resonances occur, although secondarily, are also affected by boundary conditions and sub-structure relation to the host structure. In the following section, the role of boundary conditions in the definition of the free vibrations problem solved by FEM and host structure relation is investigated.

5.1. FEM modeling in ultrasonic guided waves-vibrational modes coupling

FEM was used to calculate the natural modes and frequencies of vibration of the sub-waveguide, as detailed in the Appendix. The boundary conditions used in the FEM modeling (i.e. all four edges clamped) do not accurately reflect the conditions of the sub-laminate in relation to the host plate. In practical scenarios, the back and front edges of the sub-structure are traction free, whereas the left and right edges are rigidly connected to the pristine regions of the plate. To investigate the impact of proper sub-structure representation by boundary conditions on the computed natural frequencies, this study

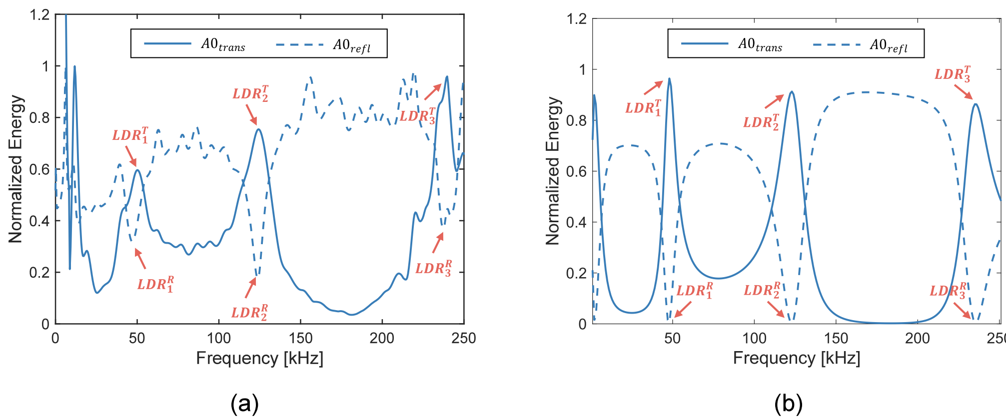

Fig. 8. Normalized scattering spectra from (a) LDV experimental tests showing LDR_1 = 48 kHz, LDR_2 = 123 kHz, LDR_3 = 237 kHz and (b) GL method showing LDR_1 = 48 kHz, LDR_2 = 123 kHz, LDR_3 = 235 kHz.

Table 3
Boundary conditions used in ABAQUS simulations.

Abbreviation	Description
CCCC	All four edges clamped
2C2F	Front and back edges clamped, left and right edges free
2F2C	Front and back edges free, left and right edges clamped
FFFF	All four edges free

explores several configurations. Shell S4R elements in ABAQUS are utilized. A study on the effect of element types is also performed by using brick C3D8 elements, on the full-clamped configuration.

Table 3 summarizes four types of boundary conditions employed in the FEM simulations. The edges refer to the sub-laminate in Fig. 3(d). Table 4 details the element types and sizes used in the Global–Local and FEM simulations, along with the corresponding computational times. The running times for the FEM analyses are computed by averaging the run times across four tests with different boundary conditions. As indicated in the table, the Global–Local method achieves faster processing time with higher resolution elements compared to FEM, while maintaining high accuracy, as evidenced in Section 4. Also notice, the Global–Local solves for the entire sub- and host structure guided wave-induced LDR problem, while the FEM analysis solves only for the natural frequencies of the sub-structure.

The natural frequencies of the first six modes of the sub-structure are computed using FEM under different boundary conditions and element types. The results along with the relative error compared to the Global–Local method are summarized in Table 5. All FEM results remain in close agreement with the Global–Local method results, with relative error below 7% overall. The relative errors are highest in the fourth mode, particularly under the 2C2F boundary conditions (error = 7.26%). Among all simulations, shell elements under 2F2C boundary conditions (front and back edges free, left and right edges clamped) exhibit the lowest relative error (4.00%) averaged across all modes. This is attributed to the consistency between these boundary conditions and the assumptions in the Global–Local analysis. Furthermore, solid elements C3D8 with all edges clamped show an average relative error of approximately 4.20%, which is higher than the lowest observed error but lower than the S4R with the same boundary conditions. Compared to shell elements with the same boundary conditions, solid element demonstrates greater precision, as expected, particularly at higher frequencies.

5.2. Effect of sub- to host structure relation on local resonances

From the characteristic equation Eq. (A.1), the resonance frequency of each mode is solely dependent on the sub-structure material and geometrical properties as:

$$f_n = \frac{1}{2\pi}\sqrt{\frac{E}{12\rho}}(\beta_n l)^2 \cdot \frac{d}{l^2} \tag{7}$$

Analytically, $\beta_n l$ is a constant for each mode, indicating that, given the material, the resonance frequency of each mode is determined by the geometric ratio d/l^2, where l is the sub-structure length (or defect length along the wave propagation direction), and d is the thickness of the sub-structure (or defect depth). Given that the LDR in ultrasonic guided wave interaction with defects arise when matching the natural frequencies of the sub-structure defined by the defect itself, such LDR frequencies only depend on the defect length and depth and not on the host structure.

Previous studies have explored the relationship between resonance frequencies and various geometric ratios such as sub-laminate-to-wavelength [23] and sub-laminate-to-plate thickness [22,55], as well as the phase difference between two sub-laminates [23,46]. The formula derived in Eq. (7) states that the resonance frequencies, hence the local resonances, are affected mainly by the thinner sub-laminate and its characteristics, regardless of its relationship with the entire plate (i.e. host) structure.

To test this proposition, a series of cases involving aluminum plates are studied: the sub-structure (i.e. thinner sub-laminate) remains unchanged (d = 0.5 mm, l = 20 mm), while the defect relationship to the host waveguide (i.e. defect type or total plate thickness) is varied. The configurations of these cases are illustrated in Table 6.

Table 7 reports the LDR frequencies of the four cases calculated by the Global–Local method and compares them with analytical solutions for natural frequencies using Eq. (7). Observations from Table 7 indicate that the local resonances exhibit similar frequency values across different configurations. Notably, Plate B, which features a notch defect compared to the delamination in Plate A, shows slightly higher resonance frequencies than Plate A, and, particularly at frequencies above 100 kHz, approaches the analytical results. Plate C and Plate D, with thicker host plates, exhibit LDR frequencies similar to those of Plate A, with the exception of the sixth mode. This may be influenced by a second group of resonances observed at 120–125 kHz in these two cases, as mentioned in Section 2. These results confirm that the main cause of the LDR phenomenon is the matching of guided waves trapped modes to natural modes of the sub-waveguide. The host waveguide characteristics (thickness, effective rigidity, mass), although secondarily, also influence LDR and the value of the frequencies at which it manifests.

Table 4
Element types, sizes, and running times in Global–Local and ABAQUS simulations.

Method	Element type	Element size (mm)	Running time (s (min))
GL	2D QUAD4	dx = dz = 0.05	1170 (19.50)
FEM	S4R	dx = dy = 0.25	2290 (38.17)
FEM	C3D8	dx = dy = 0.2, dz = 0.1	14,742 (245.70)

Table 5
Comparison of natural frequencies (kHz) of sub-structure (l = 20 mm, d = 0.5 mm) calculated with full FEM analyses for different boundary conditions and element types (relative error is calculated with respect to LDR frequencies by GL analyses with frequency step df = 0.1 kHz).

Mode	S4R - CCCC		S4R - 2C2F		S4R - 2F2C		S4R - FFFF		C3D8 - CCCC	
	f (kHz)	error	f (kHz)	error	f (kHz)	error	f (kHz)	error	f (kHz)	error
1	6.80	2.81%	6.82	2.52%	6.79	3.04%	6.79	3.07%	6.77	3.34%
2	18.65	3.02%	18.72	3.43%	18.59	2.73%	18.65	3.02%	18.58	2.64%
3	36.29	5.80%	36.48	6.36%	36.18	5.48%	36.40	6.11%	36.21	5.56%
4	59.46	6.55%	59.85	7.26%	59.26	6.20%	59.64	6.89%	59.38	6.41%
5	87.89	4.26%	88.59	5.09%	87.58	3.90%	87.77	4.12%	87.83	4.19%
6	121.31	3.07%	122.42	4.01%	120.87	2.69%	121.72	3.41%	121.26	3.02%

Table 6
Comparison of host structures with different defect types and thickness configurations.

Plate	Defect type	Configuration	Defect thickness t	Host plate thickness h
Plate A	delamination	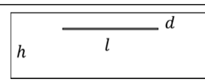	infinitesimal	2 mm
Plate B	notch	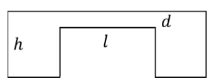	1.5 mm (open)	2 mm
Plate C	delamination	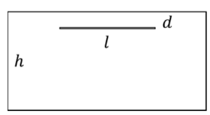	infinitesimal	3 mm
Plate D	internal void	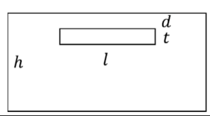	0.5 mm	3 mm

Table 7
LDR frequencies (kHz) of plates with fixed thinner sub-structure and varying defect or total plate thickness compared with natural frequencies by analytical solutions (fixed sub-structure d = 0.5 mm, l = 20 mm) in local zone of GL method).

Mode	Plate A	Plate B	Plate C	Plate D	Analytical
1	7	7	7	7	6
2	18	19	18	18	18
3	34	37	34	35	35
4	56	59	57	57	58
5	84	88	85	86	87
6	118	121	113	111	121
7	154	156	151	151	161
8	194	199	192	193	207

6. Conclusions

This work investigates the existence of LDR in UGW propagation for isotropic elastic plates with horizontal defects and clarifies its governing mechanism: LDR arises from coupling between ultrasonic guided modes of the host structure and the normal vibration modes of the sub-structure, defined by the defect, activated when the defect length is an odd multiple of a quarter wavelength. The hybrid Global–Local method computes broadband scattering spectra with high accuracy and reduced cost, capturing the characteristic full reflection/transmission at LDR frequencies while avoiding restrictive boundary idealizations of purely analytical methods.

Experimental measurements using LDV scanning on a notched aluminum plate confirm the presence of LDR frequencies and show excellent agreement with GL numerical simulations in both dispersion curves and scattering spectra. Notably, these LDR features are measurable away from the defect, enabling remote characterization, and demonstrate sensitivity to damage as small as a 6.5 mm notch, underscoring applicability to NDE/SHM.

The fundamental behavior of LDR occurrence in defected plate structures is primarily determined by the thinner sub-laminate's characteristics (length and depth). The observed shifts in LDR frequencies are due to the secondary effect of the relationship between the sub-structure and the host structure. Appropriate definition of boundary conditions for determining natural frequencies is also needed to capture the conditions of UGW to normal modes coupling. An improved agreement is expected with the adoption of higher-order beam theories in analytical analysis. Kirchhoff plate solutions can also improve agreement of analytical solutions with FEM, for natural frequencies, and an expanded 3D Global–Local solution, for UGW resonance frequencies.

Importantly, LDR manifests in transmission and reflection spectra measured away from the defect, enabling detection and characterization without prior knowledge of damage location. Building on this mechanistic foundation, a comprehensive, quantitative inversion from LDR features to defect characteristics, including size, location and type across isotropic and composite plates will require broader parametric analyses and additional experimental validation for useful NDE/SHM applications. These efforts are in progress and will be presented in subsequent publications.

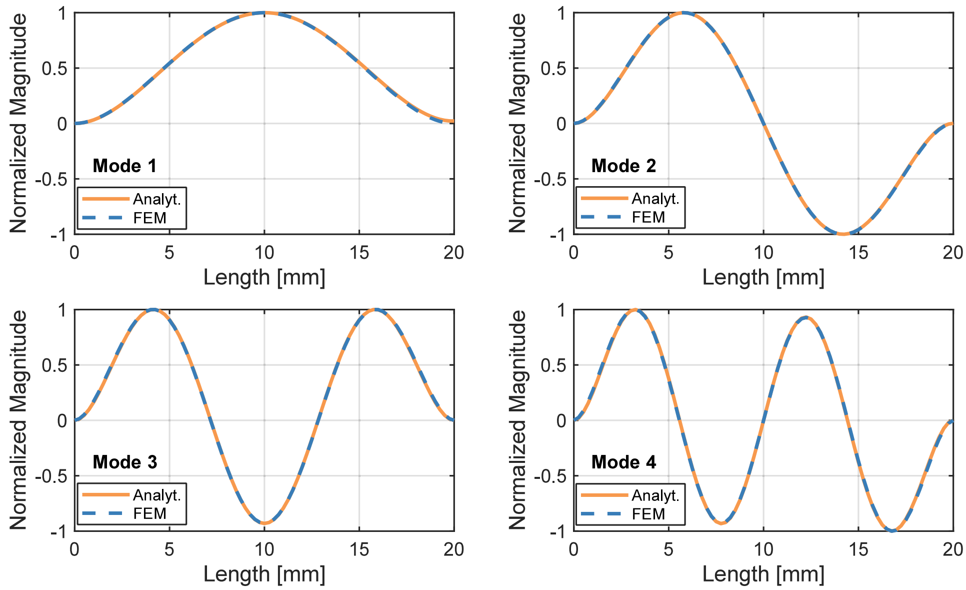

Fig. A.9. Mode shapes for the first four modes of the sub-structure obtained from analytical solution (orange solid) and FEM simulation (blue dashed). The natural frequencies for the first four modes (analytical solution) are: 6.50 kHz (Mode 1), 17.91 kHz (Mode 2), 35.10 kHz (Mode 3), and 58.02 kHz (Mode 4).

CRediT authorship contribution statement

Mingyue Zhang: Writing – original draft, Visualization, Validation, Methodology, Investigation. **Sandrine Tahina Rakotonarivo:** Writing – review & editing, Validation, Resources, Methodology. **Antonino Spada:** Writing – review & editing, Validation, Methodology, Investigation. **Margherita Capriotti:** Writing – review & editing, Writing – original draft, Supervision, Methodology, Investigation, Conceptualization.

Declaration of competing interest

The authors declare that they have no known competing financial interests or personal relationships that could have appeared to influence the work reported in this paper.

Acknowledgments

The authors acknowledge the Marine Physical Laboratory (UCSD) for the availability and access to the LDV resources, and Prof. L. Demasi (San Diego State University) for the helpful discussions. This work was also partially funded by the startup package at San Diego State University.

Appendix. Normal modes of free vibrations in sub-structures

The 1D analytical solution for a two-end fixed Euler–Bernoulli beam is used to compute the lateral vibrations of the sub-structure, which is geometrically defined by the defect (delamination in this case), under plane strain conditions. Fig. 3(a) shows the full 3D problem where the defect defines the highlighted sub-structure within the host structure. Fig. 3(b) shows the corresponding Global–Local modeling (2D). The sub-structure in this configuration is referred to as thinner sub-laminate. The choice of the Euler–Bernoulli beam Fig. 3(c) to represent the sub-structure is motivated by the study of a 2D rectangular section of an infinite 3D plate, where the thickness of the sub-structure is very small compared to its length. The natural frequencies of the beam are determined using the following equation [56]:

$$\cosh(\beta_n l)\cos(\beta_n l) - 1 = 0 \tag{A.1}$$

where l is the length of the beam, and the wavenumber for the nth mode is $\beta_n = \sqrt[4]{\frac{\omega_n^2 \rho A}{EI}}$.

In this expression, ω_n is the natural frequency (in radians) for the nth mode, ρ is the material density, A is the cross-sectional area of the sub-structure in the (y-z) plane, E is the elastic modulus, and I is the second moment of area.

The mode shapes corresponding to the normal modes are computed using the following analytical expression [56]:

$$W_n(x) = C_n\left[\sinh(\beta_n x) - \sin(\beta_n x) + \alpha_n(\cosh(\beta_n x) - \cos(\beta_n x))\right] \tag{A.2}$$

where

$$\alpha_n = \frac{\sinh(\beta_n l) - \sin(\beta_n l)}{\cos(\beta_n l) - \cosh(\beta_n l)} \tag{A.3}$$

and where C_n is typically chosen such that the maximum value of $W_n(x)$ is normalized, often to 1 for visualization purposes. The solutions are shown in Fig. A.9 in terms of natural frequencies and mode shapes (dashed orange line), for the first four modes.

This analytical approach provides a theoretical basis for understanding the vibrational characteristics of the sub-structure (sub-laminate in this case). A similar methodology was also applied by Munian [23].

To complement the analytical study, numerical simulations are conducted using the finite element method (FEM), with the software ABAQUS. The sub-laminate is here modeled in 3D, as depicted in Fig. 3(d). In alignment with the assumption of the Global–Local 2D model (Fig. 3(b)), the sub-laminate is considered to be infinitely extended in the y-direction. Practically, the width of the sub-laminate in the y-direction is set as 500 mm, a dimension that is 25 times greater than the beam's length in the x-direction, remarkably longer compared to the dimensions in the other two directions.

S4R shell elements, dx = dy = 0.25 mm, are chosen for their suitability in simulating thin structures under plane strain conditions. All edges of the sub-laminate are clamped to replicate fixed boundary conditions. The natural frequencies of the sub-laminate's normal modes are then computed using the Lanczos eigensolver, providing the vibrational behavior of the structure.

The mode shapes and natural frequencies of the first four normal modes obtained from the finite element simulations (dashed blue) are presented in Fig. A.9 and are overlapped to the ones obtained by the analytical solution (solid orange, Eq. (A.2)). These figures illustrate the vibrational patterns of the sub-laminate at its natural frequencies for the first four modes. The comparison between the theoretical calculations and numerical results proves to be nearly identical, as expected.

Data availability

Data will be made available on request.

References

[1] J.L. Rose, Ultrasonic Guided Waves in Solid Media, Cambridge University Press, 2014.
[2] C.J. Lissenden, Nonlinear ultrasonic guided waves—Principles for nondestructive evaluation, J. Appl. Phys. 129 (2) (2021).
[3] M.F. Müller, J.-Y. Kim, J. Qu, L.J. Jacobs, Characteristics of second harmonic generation of lamb waves in nonlinear elastic plates, J. Acoust. Soc. Am. 127 (4) (2010) 2141–2152.
[4] Y. Liu, V.K. Chillara, C.J. Lissenden, On selection of primary modes for generation of strong internally resonant second harmonics in plate, J. Sound Vib. 332 (19) (2013) 4517–4528.
[5] C. Prada, D. Clorennec, D. Royer, Local vibration of an elastic plate and zero-group velocity lamb modes, J. Acoust. Soc. Am. 124 (1) (2008) 203–212.
[6] Y. Wu, R. Cui, K. Zhang, X. Zhu, J.S. Popovics, On the existence of zero-group velocity modes in free rails: Modeling and experiments, NDT E Int. 132 (2022) 102727.
[7] J. Postnova, R.V. Craster, Trapped modes in elastic plates, ocean and quantum waveguides, Wave Motion 45 (4) (2008) 565–579.
[8] E. Glushkov, N. Glushkova, M. Golub, A. Boström, Natural resonance frequencies, wave blocking, and energy localization in an elastic half-space and waveguide with a crack, J. Acoust. Soc. Am. 119 (6) (2006) 3589–3598.
[9] I. Solodov, M. Kreutzbruck, Ultrasonic frequency mixing via local defect resonance for defect imaging in composites, Ultrasonics 108 (2020) 106221.
[10] X. Yu, M. Ratassepp, Z. Fan, Damage detection in quasi-isotropic composite bends using ultrasonic feature guided waves, Compos. Sci. Technol. 141 (2017) 120–129.
[11] Z. Tian, L. Yu, C. Leckey, J. Seebo, Guided wave imaging for detection and evaluation of impact-induced delamination in composites, Smart Mater. Struct. 24 (10) (2015) 105019.
[12] S. Rokhlin, Resonance phenomena of lamb waves scattering by a finite crack in a solid layer, J. Acoust. Soc. Am. 69 (4) (1981) 922–928.
[13] I. Solodov, J. Bai, S. Bekgulyan, G. Busse, A local defect resonance to enhance acoustic wave-defect interaction in ultrasonic nondestructive evaluation, Appl. Phys. Lett. 99 (21) (2011).
[14] I. Solodov, M. Rahammer, M. Kreutzbruck, Analytical evaluation of resonance frequencies for planar defects: Effect of a defect shape, NDT E Int. 102 (2019) 274–280.
[15] I. Solodov, M. Kreutzbruck, Single-sided access remote imaging via resonant airborne activation of damage, NDT E Int. 107 (2019) 102146.
[16] D. Evans, C. Linton, Trapped modes in open channels, J. Fluid Mech. 225 (1991) 153–175.
[17] D. Evans, Trapped acoustic modes, IMA J. Appl. Math. 49 (1) (1992) 45–60.
[18] D. Evans, C. Linton, F. Ursell, Trapped mode frequencies embedded in the continuous spectrum, Quart. J. Mech. Appl. Math. 46 (2) (1993) 253–274.
[19] R. Porter, D.V. Evans, Trapped modes due to narrow cracks in thin simply-supported elastic plates, Wave Motion 51 (3) (2014) 533–546.
[20] B. Poddar, V. Giurgiutiu, Complex modes expansion with vector projection using power flow to simulate lamb waves scattering from horizontal cracks and disbonds, J. Acoust. Soc. Am. 140 (3) (2016) 2123–2133.
[21] Z. Li, J. Jiao, L. Li, C. He, B. Wu, Numerical and experimental investigation on debonding detection in honeycomb sandwich using air-coupled local defect resonance and coda wave analysis, Ultrasonics 144 (2024) 107440.
[22] A. Eremin, M. Golub, E. Glushkov, N. Glushkova, Identification of delamination based on the lamb wave scattering resonance frequencies, NDT E Int. 103 (2019) 145–153.
[23] R.K. Munian, D.R. Mahapatra, S. Gopalakrishnan, Lamb wave interaction with composite delamination, Compos. Struct. 206 (2018) 484–498.
[24] K. Wang, Z. Luo, S. Xu, W. Lai, R. Guan, Q. Liu, M. Liu, J. Rao, X. Qing, Analytical insight into local defect resonance induced by disbond in multilayered structures, NDT E Int. 141 (2024) 102976.
[25] M.V. Golub, A.A. Eremin, A.N. Shpak, R. Lammering, Lamb wave scattering, conversion and resonances in an elastic layered waveguide with a surface-bonded rectangular block, Appl. Acoust. 155 (2019) 442–452.
[26] M. Šofer, Resonance phenomena of lamb waves scattering by a horizontal crack of finite length, J. Sound Vib. 490 (2021) 115742.
[27] Z. Lan, O. Saito, Y. Okabe, An insight on local defect resonance based on modal decomposition analysis: A two-dimensional case, J. Sound Vib. 596 (2025) 118718.
[28] L.H. Tenek, E.G. Henneke II, M.D. Gunzburger, Vibration of delaminated composite plates and some applications to non-destructive testing, Compos. Struct. 23 (3) (1993) 253–262.
[29] E. Glushkov, N. Glushkova, M.V. Golub, J. Moll, C.-P. Fritzen, Wave energy trapping and localization in a plate with a delamination, Smart Mater. Struct. 21 (12) (2012) 125001.
[30] E. Glushkov, N. Glushkova, A. Eremin, R. Lammering, Trapped mode effects in notched plate-like structures, J. Sound Vib. 358 (2015) 142–151.
[31] J. Segers, S. Hedayatrasa, G. Poelman, W. Van Paepegem, M. Kersemans, Probing the limits of full-field linear local defect resonance identification for deep defect detection, Ultrasonics 105 (2020) 106130.
[32] H. Mei, A. Migot, M.F. Haider, R. Joseph, M.Y. Bhuiyan, V. Giurgiutiu, Vibration-based in-situ detection and quantification of delamination in composite plates, Sensors 19 (7) (2019) 1734.
[33] Z. Tian, L. Yu, C. Leckey, Delamination detection and quantification on laminated composite structures with lamb waves and wavenumber analysis, J. Intell. Mater. Syst. Struct. 26 (13) (2015) 1723–1738.
[34] I. Solodov, M. Kreutzbruck, Local defect resonance of a through-thickness crack, Ultrasonics 118 (2022) 106565.
[35] A. Mal, Z. Chang, A semi-numerical method for elastic wave scattering calculations, Geophys. J. Int. 143 (2) (2000) 328–334.
[36] A. Spada, M. Capriotti, F.L. di Scalea, Global-local model for guided wave scattering problems with application to defect characterization in built-up composite structures, Int. J. Solids Struct. 182 (2020) 267–280.
[37] J. Ryue, D. Thompson, P. White, D. Thompson, Wave reflection and transmission due to defects in infinite structural waveguides at high frequencies, J. Sound Vib. 330 (8) (2011) 1737–1753.
[38] B. Hosten, L. Moreau, M. Castaings, Reflection and transmission coefficients for guided waves reflected by defects in viscoelastic material plates, J. Acoust. Soc. Am. 121 (6) (2007) 3409–3417.
[39] M.V. Golub, A.N. Shpak, Semi-analytical hybrid approach for the simulation of layered waveguide with a partially debonded piezoelectric structure, Appl. Math. Model. 65 (2019) 234–255.
[40] M. Zhang, L.W.E. Galvis, A. Spada, M. Capriotti, Ultrasonic guided wave scattering spectra by hybrid global–local modeling for nondestructive evaluation in composites with varying defect features, J. Nondestruct. Eval. Diagn. Progn. Eng. Syst. 7 (3) (2024) 031001.
[41] A. Spada, M. Zhang, F. Lanza di Scalea, M. Capriotti, The role of evanescent modes in global-local analysis of ultrasonic guided waves in plates with varying local zone-scatterer relations, J. Vib. Control (2023).
[42] I. Bartoli, A. Marzani, F.L. Di Scalea, E. Viola, Modeling wave propagation in damped waveguides of arbitrary cross-section, J. Sound Vib. 295 (3–5) (2006) 685–707.
[43] H. Mei, M.F. Haider, R. James, V. Giurgiutiu, Pure S0 and SH0 detections of various damage types in aerospace composites, Compos. Part B: Eng. 189 (2020) 107906.
[44] C. Ramadas, K. Balasubramaniam, M. Joshi, C.V. Krishnamurthy, Interaction of the primary anti-symmetric lamb mode (ao) with symmetric delaminations: numerical and experimental studies, Smart Mater. Struct. 18 (8) (2009) 085011.
[45] B. Feng, A.L. Ribeiro, H.G. Ramos, Interaction of lamb waves with the edges of a delamination in cfrp composites and a reference-free localization method for delamination, Measurement 122 (2018) 424–431.
[46] T. Hayashi, K. Kawashima, Multiple reflections of lamb waves at a delamination, Ultrasonics 40 (1–8) (2002) 193–197.
[47] C. Ramadas, K. Balasubramaniam, M. Joshi, C. Krishnamurthy, Numerical and experimental studies on propagation of A0 mode in a composite plate containing semi-infinite delamination: Observation of turning modes, Compos. Struct. 93 (7) (2011) 1929–1938.
[48] T. Gao, X. Liu, J. Zhu, B. Zhao, X. Qing, Multi-frequency localized wave energy for delamination identification using laser ultrasonic guided wave, Ultrasonics 116 (2021) 106486.
[49] J. Segers, S. Hedayatrasa, G. Poelman, W. Van Paepegem, M. Kersemans, Backside delamination detection in composites through local defect resonance induced nonlinear source behavior, J. Sound Vib. 479 (2020) 115360.
[50] P.D. Juarez, C.A. Leckey, Multi-frequency local wavenumber analysis and ply correlation of delamination damage, Ultrasonics 62 (2015) 56–65.
[51] M.V. Golub, A.A. Eremin, E.V. Glushkov, N.V. Glushkova, Guided wave resonance identification of interface delamination in bimaterial composites, Compos. Struct. 334 (2024) 117983.
[52] M. Ruzzene, Frequency–wavenumber domain filtering for improved damage visualization, Smart Mater. Struct. 16 (6) (2007) 2116.
[53] T.E. Michaels, J.E. Michaels, M. Ruzzene, Frequency–wavenumber domain analysis of guided wavefields, Ultrasonics 51 (4) (2011) 452–466.
[54] M.D. Rogge, C.A. Leckey, Characterization of impact damage in composite laminates using guided wavefield imaging and local wavenumber domain analysis, Ultrasonics 53 (7) (2013) 1217–1226.
[55] N. Guo, P. Cawley, The interaction of lamb waves with delaminations in composite laminates, J. Acoust. Soc. Am. 94 (4) (1993) 2240–2246.
[56] S.S. Rao, F.F. Yap, Mechanical Vibrations, vol. 4, Addison-Wesley New York, 1995.